THE ASTROPHYSICAL JOURNAL, 493:54–61, 1998 January 20

A MEDIUM SURVEY OF THE HARD X-RAY SKY WITH THE *ASCA* GAS IMAGING SPECTROMETER: THE (2–10 keV) NUMBER COUNTS RELATIONSHIP

I. CAGNONI,[1,2,3] R. DELLA CECA,[4,5] AND T. MACCACARO[4,6]

Received 1997 February 24; accepted 1997 September 2

ABSTRACT

In this paper, we report the first results of a medium survey program conducted in the 2–10 keV energy band using data from the GIS2 instrument onboard the *ASCA* satellite.

We have selected from the *ASCA* public archive (as of 1996 February 14) 87 images suitable for this project. Sixty serendipitous X-ray sources with a signal-to-noise ratio greater than 3.5 were found. The 2–10 keV flux of the detected sources ranges from $\sim 1.1 \times 10^{-13}$ ergs cm^{-2} s^{-1} to $\sim 4.1 \times 10^{-12}$ ergs cm^{-2} s^{-1}.

Using this sample, we have extended the description of the 2–10 keV log $N(>S)$–log S to a flux limit of $\sim 6.3 \times 10^{-14}$ ergs cm^{-2} s^{-1} (the faintest detectable flux), i.e., about 2.7 orders of magnitude fainter than the Piccinotti et al. determination. The derived number-flux relationship is well described by a power-law model, $N(>S) = K \times S^{-\alpha}$, with best-fit values $\alpha = 1.67 \pm 0.18$ and $K = 2.85 \times 10^{-21}$ deg^{-2}.

At the flux limit of the survey, about 27% of the cosmic X-ray background in the 2–10 keV energy band is resolved in discrete sources. A flattening of the number-flux relationship, within a factor of 10 from the flux limit of the present survey, is expected in order to avoid saturation.

The implications of these results for models of the origin of the hard X-ray background are briefly discussed.

Subject headings: diffuse radiation — surveys — X-rays: galaxies — X-rays: general

1. INTRODUCTION

The origin of the cosmic X-ray background (CXB), discovered almost 35 yr ago (Giacconi et al. 1962), represents one of the long-standing problems of modern cosmology (see reviews by Fabian & Barcons 1992; Setti & Comastri 1996).

The very small deviation of the cosmic microwave background spectrum from a blackbody shape seems to have put to rest the suggestion that a significant fraction of the CXB is due to truly diffuse emission from a hot intergalactic medium (Mather et al. 1994). Only the alternative interpretation, a discrete sources origin, is left.

X-ray surveys provide a powerful tool for studying the nature and properties of the classes of X-ray emitters that produce the CXB. In the soft X-ray energy band ($E < 2$ keV), where grazing incidence focusing optics have been used, deep surveys conducted with the *ROSAT* observatory (Hasinger et al. 1993; Branduardi-Raymont et al. 1994; Vikhilin et al. 1995) have revealed a surface density of X-ray sources of ~ 415 deg^{-2} at a flux limit of 2.5×10^{-15} ergs cm^{-2} s^{-1} (0.5–2.0 keV), contributing $\sim 60\%$–65% of the CXB in the same energy band. The differential log N–log S can be described (see, e.g., Hasinger et al. 1993) by a broken power law model with a slope of ~ 1.85 for $S \lesssim 2.2 \times 10^{-14}$ ergs cm^{-2} s^{-1} and ~ 2.6 for $S \gtrsim 2.2 \times 10^{-14}$ ergs cm^{-2} s^{-1}. At brighter fluxes, a good agreement is found with the surface density previously obtained using data from the *Einstein Observatory* (Primini et al. 1991; Gioia et al. 1990).

Spectroscopic observations of the *ROSAT* sources, along with the results obtained by the *Einstein* Extended Medium-Sensitivity Survey identification program (EMSS; Gioia et al. 1990; Stocke et al. 1991; Maccacaro et al. 1994), have allowed us to clarify the nature and composition of the sources that shine in the soft X-ray sky.

Broad-line AGNs constitute the majority of the soft X-ray sources at the fluxes actually sampled; they represent $\sim 50\%$ of the sources in the EMSS ($\langle z \rangle \simeq 0.4$) and $\sim 50\%$–60% of the *ROSAT* sources with $S \gtrsim 5$–6×10^{-15} ergs cm^{-2} s^{-1} ($\langle z \rangle \simeq 1.5$; Shanks et al. 1991; Boyle et al. 1993, 1994, 1995; Jones et al. 1997).

Clusters of galaxies are the next most numerous class of extragalactic sources in bright X-ray surveys. At $S \geq 1 \times 10^{-13}$ ergs cm^{-2} s^{-1}, for example, they represent $\sim 13\%$ of the sources in the EMSS. However, they become less important as one moves toward fainter fluxes (Rosati et al. 1995).

An important minority ($\sim 10\%$) of the *ROSAT* sources are spectroscopically identified with X-ray luminous galaxies, consisting of both early-type and narrow emission line galaxies (Griffiths et al. 1995, 1996). According to their cosmological evolution properties (Griffiths et al. 1996), these objects could become increasingly more important at fainter fluxes and could constitute a significant fraction of the largely unidentified sources present at the *ROSAT* deep survey flux limit. The real nature of these objects (obscured AGNs? starburst galaxies?) is at the moment unclear.

Based on studies of the cosmological properties of the known classes of objects, it is now evident that their combined contribution to the soft CXB is approaching 100% (see, e.g., for broad-line AGN, Boyle et al. 1993, 1994; Jones et al. 1997; for clusters of galaxies, Rosati et al. 1995; for X-ray luminous galaxies, Boyle et al. 1995; Griffiths et al. 1995, 1996).

In contrast, our knowledge of the nature and composition of the sources that produce the 2–10 keV CXB, closer

[1] Università degli Studi di Milano, Via Celoria 16, 20133, Milano, Italy.
[2] Harvard-Smithsonian Center for Astrophysics, 60 Garden Street, Cambridge, MA 02138.
[3] ilaria@alessandro.harvard.edu.
[4] Osservatorio Astronomico di Brera, Via Brera 28, 20121 Milano, Italy.
[5] rdc@brera.mi.astro.it.
[6] tommaso@brera.mi.astro.it.

to where the bulk of the energy density resides, is quite scanty. Before *ASCA*, surveys in this energy range were made using passively collimated X-ray detectors. These instruments were able to accurately measure the CXB spectrum (which is remarkably well fitted by a thermal bremsstrahlung model with a temperature of the order of 40 keV; see Marshall et al. 1980; Gruber 1992) but because of limited spatial resolution, they were only able to resolve the brightest X-ray sources, which represent only a small fraction ($<5\%$) of the CXB.

The only statistically complete large sample of X-ray sources in the 2–10 keV energy band was obtained from the A-2 experiment on *HEAO 1* (Piccinotti et al. 1982). This sample is composed of 85 sources (excluding the LMC and SMC) brighter than $\sim 3.1 \times 10^{-11}$ ergs cm^{-2} s^{-1}, found in ~ 8.2 sr of the sky at $|b| > 20°$. Of the 62 sources of extragalactic origin, about half are AGNs and half are clusters of galaxies.

Source counts down to a flux of $\sim 8 \times 10^{-12}$ ergs cm^{-2} s^{-1} were obtained by Kondo (1991) using data from the *Ginga* satellite. A small sample of 11 sources was derived from an analysis of 383 deg^2.

The *Ginga* fluctuations analysis (Warwick & Stewart 1989; Butcher et al. 1997) extend the study of the number-flux relationship to a flux on the order of $\sim 10^{-13}$ ergs cm^{-2} s^{-1}. However, these studies are model dependent (the spectral and clustering properties of the sources have to be assumed) and do not give direct indications of the intrinsic nature of the X-ray emitters responsible for the CXB.

The so-called spectral paradox, i.e., that none of the single classes of known X-ray emitters is characterized by an energy spectral distribution similar to that of the CXB, further complicates the situation.

Given this frustrating state of affairs, a method for deriving the contribution of the different classes of X-ray sources to the hard CXB through population synthesis models was developed (using average broadband spectral properties folded with cosmological evolution properties determined in the soft X-ray energy band). Among the proposed classes of X-ray emitters that could be important for the production of the hard CXB, are reflection-dominated AGNs (see Fabian 1989; Zdziarski et al. 1993 and reference therein), strongly absorbed AGNs (Setti & Woltjer 1989; Madau, Ghisellini, & Fabian 1994; Comastri et al. 1995) and starburst galaxies (Griffiths & Padovani 1990).

It is clear that a direct measurement, through selection of a sample of hard X-ray emitters, is therefore crucial to test competing models.

The *ASCA* satellite is carrying the first imaging instrument in the 2–10 keV energy band. This gives us the ability to determine the surface density of hard X-ray–selected sources to $\lesssim 10^{-13}$ ergs cm^{-2} s^{-1} directly from the source counts and to clarify the nature of the X-ray emitters responsible for the hard CXB through optical spectroscopic follow-up observations.

In this paper, we report first results of a medium-survey program in the 2–10 keV energy range using data from the GIS2 instrument onboard the *ASCA* observatory. The paper is organized as follows. In § 2, we discuss the criteria for the selection and construction of the images used, for the selection of the sources, and for the definition of the sky coverage. In § 3, we report the main result obtained so far, the number counts relationship, derived directly from source counts, down to a flux limit of $\sim 6.3 \times 10^{-14}$ ergs cm^{-2} s^{-1}. We compare this log $N(>S)$–log S with previous results from *HEAO 1* and *Ginga*, with new results obtained from other groups using *ASCA* deep survey fields, and with the extrapolation of log $N(>S)$–log S from the soft X-ray energy band. Finally, § 4 presents a discussion and conclusions.

2. SELECTION CRITERIA AND DATA ANALYSIS

ASCA (Tanaka, Inoue, & Holt 1994; Serlemitsos et al. 1995) was launched on 1993 February 20 by the Japanese Institute for Space Astronautical Science. The focal plane instrumentation consists of two solid-state imaging spectrometers (hereafter SIS0 and SIS1 or in general SIS) and two gas imaging spectrometers (hereafter GIS2 and GIS3 or in general GIS), operating simultaneously.

For the purpose of this survey, we have used the GIS2 instrument for the following reasons:

1. The GIS has a circular field of view of $\sim 50'$ diameter, ~ 4 times larger than the SIS field of view ($\sim 22' \times 22'$ when used in 4 CCD mode). Furthermore, only a limited number of *ASCA* observations were made with the SIS in the 4 CCD mode option.
2. For energies above ~ 5 keV, the effective area of the GIS is larger than the effective area of the SIS.
3. The GIS2 detector has a larger area uncontaminated by high non–X-ray background than the GIS3 (see *ASCA* guest investigator program, Announcement of Opportunity *EAO-1*, 1993 December 17).

2.1. *ASCA Field Selection and GIS2 Cleaning Parameters*

The *ASCA* public data considered here were extracted from the public archive (as of 1996 February 14).

We have excluded from the survey those fields centered on:

1. $|b| < 20$
2. Targets in the Large and Small Magellanic Clouds.
3. Very bright (see § 2.4) and/or extended targets, e.g., supernovae remnants, very rich, and nearby clusters of galaxies.
4. Groups and/or associations of targets, e.g., groups of nearby galaxies, star clusters, or stellar associations.

All these selection criteria were applied to avoid regions of high Galactic absorption and high stellar density, to dismiss images where the background map (see § 2.2) could not be produced reliably, and to prevent inclusion in the survey of sources not truly serendipitous (e.g., physically related to the target). We have also excluded from the analysis images with exposure times (after data cleaning; see below) of $<10{,}000$ s, since their sensitivity is so poor that they do not significantly contribute to the sky coverage of the survey. Finally, in the case of two or more overlapping images we have retained only the deepest one.

A total of 87 GIS2 fields (listed in Table 1) survive these selection criteria.

Image preparation has been performed using version 1.2 of the XSELECT software package and version 3.2 of FTOOLS. Good time intervals were selected by applying standard cleaning criteria, the most relevant being a magnetic cutoff rigidity threshold of 6 GeV c^{-1} and a minimum elevation angle of 6°. We have also excluded from the analysis periods of time that are within 60 s of the South Atlantic Anomaly passage and within 100 s of the day/night

TABLE 1

LIST OF *ASCA* FIELDS USED

Target Name	Sequence No.	α^a	δ^a	T_{exp} (s)
β Ceti	21019000	00 43 37.0	−18 03 56	19977
GSGP 4	92005000	00 57 29.8	−27 37 20	36934
GRB 191178	22034000	01 18 40.2	−28 39 14	27160
NGC 507	61007000	01 23 03.3	+33 20 00	37591
NGC 720	60004000	01 53 19.0	−13 42 27	34213
Mrk 1040	72016000	02 28 23.0	+31 22 15	19853
PHL 1377	72031000	02 35 17.9	−03 57 21	31683
AO 0235+164	71015020	02 38 30.0	+16 32 02	24858
A370	80010000	02 39 58.5	−01 31 57	34812
NGC 1097	61001000	02 46 04.6	−30 18 01	36872
NGC 1313	60028000	03 18 25.9	−66 28 24	23282
NGC 1316	61002000	03 22 25.3	−37 14 18	34007
1H 0323+022	71034000	03 26 06.2	+02 20 43	34584
ϵ Eri	22009000	03 33 04.8	−09 24 12	19459
QSF 3	90011000	03 41 44.7	−44 07 06	22967
MS 0353.6−364	82042000	03 55 47.7	−36 32 12	17864
VW Hyi	31001000	04 09 59.1	−71 21 03	12132
NGC 1614	61011000	04 33 49.7	−08 39 08	32957
PKS 0438−436	70010000	04 40 22.0	−43 32 29	32569
NGC 1667	71032000	04 48 27.0	−06 23 43	38173
E0449−184	71033000	04 51 27.0	−18 23 20	36489
MSS 0451.6−03	81025000	04 54 01.2	−03 05 33	52439
MS 0451.5+02	82041000	04 54 26.4	+02 54 58	18684
NGC 1808	71031000	05 07 27.7	−37 35 17	32750
Mrk 3	70002000	06 15 25.3	+71 01 53	27640
0716+714	71006020	07 20 59.8	+71 17 46	19020
YY Gem	20002000	07 34 57.8	+31 57 55	30441
PI 1 UMa	21018000	08 39 41.5	+65 05 16	24336
Lynx Field	90009010	08 49 11.3	+44 50 08	39943
IRAS 09104	71002000	09 13 52.6	+40 56 14	38492
GL 355	21020000	09 32 46.3	−11 09 37	19166
NGC 2992	71049000	09 45 26.2	−14 22 52	25914
NGC 3079	60000000	10 01 12.4	+55 38 07	38704
3C 234	71043000	10 01 27.8	+28 45 12	16194
A963	80000000	10 16 32.6	+39 00 12	23077
NGC 3147	60040000	10 17 06.4	+73 23 25	36120
AD Leo	20006000	10 19 18.7	+19 53 44	26183
IRAS F10214+4	61003000	10 25 03.1	+47 10 34	34854
RE 1034+39	72020000	10 35 04.3	+39 40 29	28345
NGC 3310	61013000	10 38 11.3	+53 29 19	17648
Lockman Hole	90010020	10 52 08.6	+57 22 39	21593
A1204	82002000	11 12 50.6	+17 32 40	27692
NGC 3628	61015000	11 20 31.0	+13 34 19	21616
HCG 51	82028000	11 22 06.2	+24 15 02	11694
MKW 4 NE	82013000	12 05 07.2	+01 57 31	19574
NGC 4203	61008000	12 15 21.1	+33 10 22	36451
NGC 4418	62003000	12 26 35.0	+00 54 59	25875
MS 1224.7+200	82043000	12 27 04.1	+19 53 02	11533
NGC 4449	62011000	12 27 43.0	+44 05 25	45021
NGC 4472 NW8	60030000	12 29 23.1	+07 54 16	20128
NGC 4643	62001000	12 42 52.3	+01 55 56	35222
NGC 4649	61005000	12 43 54.0	+11 31 37	25447
MS 1248.7+570	72032000	12 50 21.8	+56 49 13	31492
GP Com	32002000	13 05 22.3	+17 58 54	29922
NGC 4968	71039000	13 07 28.3	−23 39 01	25755
LSS Line C-P	92002070	13 13 02.9	+31 21 36	16928
A1704	81007000	13 13 50.6	+64 38 19	18570
A1722	81013000	13 19 53.5	+70 05 20	39580
NGC 5236	61016000	13 37 04.3	−29 52 08	10474
NGC 5252	71021000	13 38 33.6	+04 35 08	67795
CL 1358+6245	81032000	13 59 23.3	+62 35 28	35062
K416	62007000	14 05 51.4	+50 44 56	33977
PG 1404+226	72021000	14 06 07.0	+22 22 52	25639
PKS 1404−267	81019000	14 07 53.0	−26 59 12	34280
PG 1407+265	70024000	14 08 54.4	+26 16 19	23344
3C 295	71003000	14 11 00.0	+52 14 40	44926
MS 1426.4+01	82044000	14 28 46.8	+01 46 41	18734
NGC 5695	71009000	14 37 39.8	+36 34 09	24626
HD 129333	22012000	14 38 16.6	+64 19 39	19008
NGC 5846	61012000	15 06 37.4	+01 36 39	39548
3C 313	71004000	15 11 17.3	+07 54 21	41082
Arp 220	60035000	15 34 29.7	+23 27 42	33031
PG 1634+706	71036000	16 34 25.0	+70 35 27	38496
A2218	80001000	16 35 56.6	+66 15 38	23913
A2219	82037000	16 39 42.7	+46 40 27	33941
NGC 6240	71022000	16 53 13.2	+02 28 15	31539
Dra 3	90024000	17 10 24.2	+71 06 07	33590
PG 1718+481	71037000	17 19 38.6	+48 08 07	33194
Nep Field 1	90020000	17 59 59.8	+66 33 48	21718
Pavo Group	81020000	20 18 33.1	−70 51 12	30942
PKS 2126−158	70014000	21 29 20.4	−15 34 58	11044
MS 2137.3−235	81022000	21 40 29.0	−23 38 35	16794
A2440	81033000	22 23 43.2	−01 37 15	36602
PHL 5200	72033000	22 28 37.7	−05 13 42	13130
IC 1459	60005000	22 57 15.6	−36 27 23	27002
DI Peg	22002000	23 32 21.8	+15 03 11	33458
A2670	82049000	23 54 30.2	−10 19 42	27628

NOTE.—Units of right ascension are hours, minutes, and seconds, and units of declination are degrees, arcminutes, and arcseconds.

[a] Equatorial coordinates; equinox J2000.

transition passage. Finally, images were extracted in the 2–10 keV energy range, in detector coordinates, considering only the events within 20′ of the detector center. The pixel size of these images is 15″ × 15″.

2.2. *Source Detection and Selection*

To localize and characterize the faint sources contained in the selected fields, we need to estimate the underlying background as precisely as possible. A detailed description of the properties of the GIS2 background is reported in Kubo et al. (1994) and Ikebe et al. (1995). In brief, the GIS2 background consists of non–X-ray background (NXB) and cosmic X-ray background (CXB); the first increases from the center to the edge of the detector, while the latter shows an opposite behavior.

After a detailed radial and azimuthal analysis of the background properties in 30 GIS2 images (which do not show evident X-ray sources), we reached the conclusion that the GIS2 background has a structure that is reproduced from image to image. For these reasons, we decided to use the Blank Sky event files, which include both the NXB and CXB. These Blank Sky event files have been constructed by the GIS team, summing a total of 15 separate pointings of blank fields,[7] and are publicly available.

In order to match as closely as possible the selection criteria used to extract the survey images, we have extracted Blank Sky images (hereafter BSI) in the 2–10 keV energy band, including only events with a magnetic cutoff rigidity threshold above 6.

We have then applied the following multistep procedure to each image:

1. A first estimate of the background statistics in each image has been determined in three boxes (each 5′ × 5′) that do not contain evident X-ray sources. Median values of the mean and standard deviation for these three regions have been considered ($\overline{\text{cts}}$, σ).

[7] Even if these observations do not contain bright X-ray sources, we found evidence of three faint sources; these sources have been averaged out by substituting mean values from surrounding areas.

2. Values of $\overline{\text{cts}}$ and σ have been used to define the region (hereafter BR) in each image where the counts per pixel are $\leq \overline{\text{cts}} + 2\sigma$.

3. This region has been used to produce a normalized version of the background map (hereafter BN) by rescaling the BSI according to

$$\text{BN} = \text{BSI} \times \frac{\text{total counts in each image from BR}}{\text{total counts in BSI from BR}}.$$

We have preferred to normalize the exposure map in this way, rather than by using the exposure time, because from our analysis of the 30 GIS2 images we have found that the intensity of the background rate, but not its overall structure across the field, can significantly change from image to image.

4. Each image and the corresponding BN have then been smoothed with a bidimensional Gaussian with $\sigma = 1'$, which is comparable to the "core" of the (XRT + GIS2) point-spread function (PSF).

5. The smoothed version of BN has been subtracted from the smoothed version of each image in order to obtain a background-subtracted image.

6. Contour plots in each background-subtracted image have been used to localize the contiguous pixels ("peaks") that are 0.5 σ above the local mean. The value of 0.5 σ has been determined empirically, and ensures completeness above the source detection threshold of 3.5 (see below).

7. Net counts, in a circle of 2′ radius around each of these peaks, are computed by subtracting the background counts accumulated in BN from the total counts accumulated in each image.

8. Sources are accepted as real if the signal-to-noise ratio (S/N), defined as [net counts/(net counts + background)$^{1/2}$], is greater than 3.5.

Excluding the sources related to the targets and the targets themselves, a total of 60 X-ray sources satisfy the criteria for inclusion in the survey.

In Table 2, we report the basic data for the 60 sources in the sample. We list the name, the *ASCA* sequence number where the source was found, celestial (J2000) coordinates, the signal-to-noise ratio, the corrected flux (and its error), and the Galactic N_{H} along the line of sight. We note that the absolute accuracy of the *ASCA* attitude solution is on the order of 2′.

2.3. *Correction for Vignetting and PSF*

In order to obtain the correct flux for the sources, we must now consider the position-dependent sensitivity of the GIS2 detector. In particular, we must take into account 1) the fraction of source photons falling outside the 2′ circle radius, 2) the variation in the sensitivity of the detector as a function of the distance from the optical axis due to vignetting, and 3) the variation of the (XRT + GIS2) PSF across the field of view. These effects are taken into consideration by the FTOOLS task ASCAARF, which is able to produce a position-dependent PSF-corrected effective area of the (XRT + GIS2) combination. In essence, the input of ASCAARF is the position x, y (in detector coordinates) and the dimension of the source extraction region d_r (in our case, a circle with radius 2′).

Using ASCAARF (version 2.64), we have produced a raster scan of the effective area values across the GIS2 field of view and used them (through spectral simulation with XSPEC) to obtain the count rate to flux conversion factors (f_{xy}) relative to each position x, y in the detector. In the spectral simulations, we have used a power law model with energy index 0.7, filtered by a Galactic absorbing column density of 3×10^{20} cm^{-2}. The count rate to flux conversion factors are a very weak function of the Galactic absorbing column density along the line of sight (which ranges from 10^{20} cm^{-2} to $g \times 10^{20}$ cm^{-2} for the present sample) and are accurate to $\pm 15\%$ for all the energy spectral indices in the range 0.5–1.0. The flux of each source has then been computed and is listed in Table 2.

2.4. *Sky Coverage*

The sky coverage (i.e., the area covered as a function of the flux limit) of the present survey has been determined in the following way. At each position of the raster scan of a given image, we have used the corresponding background map to compute the total counts that a source should have to be detected at the 3.5 S/N level. These counts have been converted to count rate and then to flux using the same conversion factors (f_{xy}) used for the sources.

The area associated with the target has been excluded from the sky coverage computation; to this purpose, we have considered as the target area a circle defined by the location where the expected counts from the pointed source are $\geq 15\%$ of those of the background in the corresponding background map. The circles associated with the targets range from 6′ to 10′ radius. In the case of circles greater than 12′ radius, we have excluded the whole field from the survey.

An integral representation of the sky coverage is shown in Figure 1.

The raster scan used to compute the sky coverage allows us to estimate the number of expected spurious sources in the survey. The number of background counts in BN inside a circle of 2′ radius is a function of 1) the image exposure time and 2) the circle position in the image. The background counts range between 10 and 15 for an image with an exposure time of ~ 10 ks, between 35 and 50 for an image with an exposure time of ~ 40 ks, and between 65 and 85 for an image with an exposure time of ~ 70 ks. Considering the

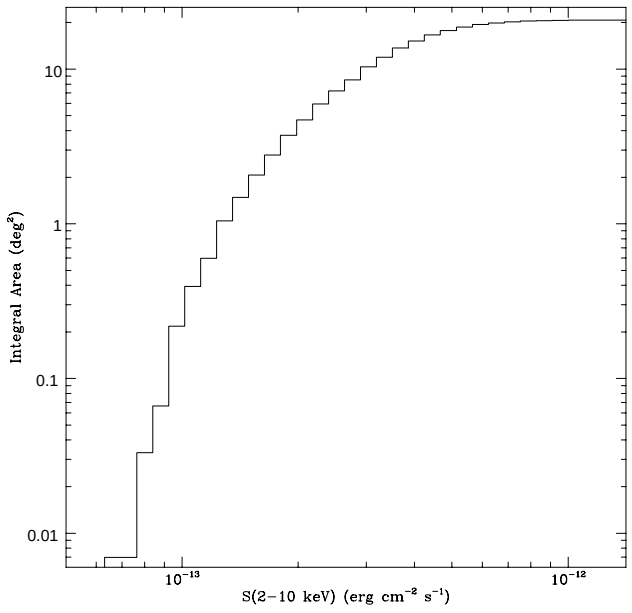

FIG. 1.—Integral sky coverage of the present survey (see text for details)

TABLE 2

THE SOURCE SAMPLE

Source Name	Sequence No.	α (J2000)	δ (J2000)	S/N	Flux (10^{-13} ergs cm^{-2} s^{-1})	Flux Error[a] (10^{-13} ergs cm^{-2} s^{-1})	N_H[b] (10^{20} cm^{-2})
a0057−2740	92005000	00 57 01.2	−27 40 58.0	3.94	2.09	0.53	1.95
a0117−2834	22034000	01 17 43.8	−28 34 41.8	4.45	3.69	0.83	1.65
a0123+3312	61007000	01 23 10.0	+33 12 43.7	5.02	3.25	0.64	4.75
a0153−1346	60004000	01 53 25.6	−13 46 56.7	3.90	1.48	0.38	1.74
a0228+3133	72016000	02 28 33.8	+31 33 15.2	14.20	23.61	1.66	9.06
a0235−0343	72031000	02 35 03.0	−03 43 16.3	3.94	2.96	0.75	3.16
a0235−0348	72031000	02 35 21.4	−03 48 21.5	6.83	4.10	0.60	3.16
a0240−0132	80010000	02 40 23.1	−01 32 05.5	4.09	1.87	0.45	4.42
a0240−0140	80010000	02 40 25.6	−01 40 13.1	3.54	2.35	0.67	3.75
a0318−6636	60028000	03 18 27.9	−66 36 47.9	18.85	41.35	2.19	3.48
a0321−3713	61002000	03 21 40.1	−37 13 41.5	3.82	1.68	0.44	2.36
a0322−3716	61002000	03 22 58.7	−37 16 48.8	3.85	1.95	0.51	2.31
a0341−4353	90011000	03 41 48.0	−43 53 47.0	4.55	4.50	0.99	1.80
a0406−7114	31001000	04 06 46.5	−71 14 42.4	3.65	9.00	2.46	5.41
a0438−4332	70010000	04 38 57.4	−43 32 20.2	4.28	4.43	1.03	2.48
a0447−0627	71032000	04 47 49.3	−06 27 31.1	5.80	3.35	0.58	6.27
a0506−3726	71031000	05 06 13.1	−37 26 47.8	5.82	6.10	1.05	2.19
a0506−3742	71031000	05 06 58.6	−37 42 06.6	5.04	3.00	0.59	2.28
a0614+7050	70002000	06 14 08.9	+70 50 32.5	4.00	3.34	0.83	8.43
a0721+7111	71006020	07 21 00.3	+71 11 48.7	5.86	5.07	0.87	5.01
a0734+3203	20002000	07 34 21.8	+32 03 38.7	3.54	1.92	0.54	5.43
a0837+6512	21018000	08 37 55.1	+65 12 07.9	6.30	7.33	1.16	4.08
a0848+4442	90009010	08 48 18.2	+44 42 33.3	4.15	2.66	0.64	3.08
a0959+5534	60000000	09 59 51.2	+55 34 52.4	4.57	3.25	0.71	1.22
a1000+5537	60000000	10 00 38.6	+55 37 28.7	6.09	2.72	0.45	1.13
a1001+5542	60000000	10 01 02.5	+55 42 53.1	5.30	2.08	0.39	1.13
a1001+5555	60000000	10 01 27.7	+55 55 03.9	5.12	7.90	1.54	1.16
a1019+7325	60040000	10 19 30.4	+73 25 26.3	5.09	3.90	0.77	2.59
a1051+5735	90010020	10 51 37.1	+57 35 53.2	4.37	4.52	1.50	0.70
a1051+5732	90010020	10 51 39.9	+57 32 53.9	4.52	5.43	0.89	0.70
a1226+1952	82043000	12 26 42.9	+19 52 32.3	7.25	8.71	1.20	1.93
a1242+0147	62001000	12 42 30.0	+01 47 29.9	3.50	1.52	0.43	1.63
a1249+5654	72032000	12 49 53.7	+56 54 30.1	3.60	1.74	0.48	1.22
a1308+2348	71039000	13 08 08.0	−23 48 58.0	3.97	4.45	1.12	5.88
a1312+3114	92002070	13 12 55.0	+31 14 21.8	3.89	2.85	0.73	1.17
a1320+7010	81013000	13 20 29.7	+70 10 07.0	4.49	1.50	0.33	1.58
a1339+0434	71021000	13 39 10.4	+04 34 18.3	4.50	1.66	0.36	2.10
a1359+6219	81032000	13 59 52.3	+62 19 22.1	5.36	7.43	1.39	1.63
a1401+6222	81032000	14 01 00.0	+62 22 34.4	7.12	11.36	1.59	1.62
a1405+5042	62007000	14 05 16.8	+50 42 19.8	5.86	2.30	0.39	1.56
a1405+2225	72021000	14 05 32.7	+22 25 00.0	6.60	5.50	0.83	2.40
a1405+5056	62007000	14 05 36.2	+50 56 57.1	5.21	3.37	0.65	1.41
a1409+2609	70024000	14 09 46.9	+26 09 26.1	4.56	5.37	1.18	1.71
a1410+5215	71003000	14 10 00.2	+52 15 53.9	3.58	1.32	0.37	1.30
a1410+5204	71003000	14 10 33.5	+52 04 21.3	4.10	2.70	0.66	1.31
a1411+5229	71003000	14 11 04.7	+52 29 40.6	3.56	2.47	0.69	1.30
a1438+3644	71009000	14 38 05.3	+36 44 28.2	3.57	3.10	0.87	1.11
a1438+3630	71009000	14 38 24.3	+36 30 39.7	5.09	4.34	0.85	1.11
a1507+0145	61012000	15 07 13.3	+01 45 10.8	4.08	2.67	0.66	3.95
a1511+0757	71004000	15 11 46.5	+07 57 48.5	7.20	4.21	0.58	3.00
a1534+2328	60035000	15 34 20.3	+23 28 22.1	3.85	1.08	0.28	4.41
a1709+7059	90024000	17 09 14.9	+70 59 29.5	3.88	1.86	0.48	3.94
a1711+7110	90024000	17 11 46.1	+71 10 50.1	5.13	2.79	0.54	3.93
a1800+6638	90020000	18 00 02.5	+66 38 46.1	7.90	6.72	0.85	5.18
a2017−7055	81020000	20 17 18.1	−70 55 17.5	4.83	3.37	0.70	5.20
a2222−0143	81033000	22 22 57.7	−01 43 19.0	8.27	6.20	0.75	5.05
a2257−3619	60005000	22 57 08.3	−36 19 57.9	3.67	1.91	0.52	1.98
a2332+1507	22002000	23 32 09.3	+15 07 24.2	3.65	1.25	0.34	3.50
a2332+1511	22002000	23 32 55.6	+15 11 53.5	11.00	10.14	0.92	3.58
a2355−1027	82049000	23 55 32.3	−10 27 29.4	6.25	10.94	1.75	3.29

NOTE.—Units of right ascension are hours, minutes, and seconds, and units of declination are degrees, arcminutes, and arcseconds.

[a] The flux error corresponds to the statistical error and has been computed using the total counts (source + background) at the position of the source in the 2′ circle radius.

[b] Computed using the GETNH program, which accesses a database containing the Stark et al. (1994) northern hemisphere H I survey and a compilation of southern hemisphere surveys.

extremes of these values, the requirement of a S/N = 3.5 implies that a minimum of 19 (39) net counts must be recorded in addition to the 10 (85) background counts. For a Poisson distribution, the probability of observing 29 (124) total counts or more when 10 (85) are expected is 7.6×10^{-7} (4.3×10^{-5}). We note that the 4 σ level in Gaussian statistics is $\sim 6 \times 10^{-5}$. The number of resolution elements of this survey is $\sim$6000 (total area divided by the

detection cell area); thus, the number of spurious sources expected is <0.3.

3. RESULTS

In Figure 2, we show a nonparametric representation of the number-flux relationship (*open circles*) obtained by folding the sky coverage with the flux of each source. Because we are primarily interested in the extragalactic number-flux relationship, we have excluded from the computation two sources (a0341−4353 and a1410+5215) that are suspected stars. In the same figure, we also report a parametric representation of the log $N(>S)$–log S (*solid line*), obtained by applying the maximum-likelihood method to the unbinned data (see Gioia et al. 1990 for details of these two representations). The fit has been performed from a flux of $\sim 6.3 \times 10^{-14}$ ergs cm^{-2} s^{-1} (the faintest detectable flux) to a flux of $\sim 10^{-11}$ ergs cm^{-2} s^{-1}. For fluxes brighter than this limit our survey may not be complete, since most of the "bright" X-ray sources were chosen as targets of observation and then excluded, by definition, from the survey. However, we note that the space density of sources with flux greater than $\sim 10^{-11}$ ergs cm^{-2} s^{-1} is such that <0.2 sources are expected in this survey. We also note that <1 source is expected with flux between $\sim 6.3 \times 10^{-14}$ ergs cm^{-2} s^{-1} and $\sim 1.1 \times 10^{-13}$ ergs cm^{-2} s^{-1} (the flux of the faintest detected source).

The log $N(>S)$–log S can be described by a power-law model, $N(>S) = K \times S^{-\alpha}$, with best-fit value for the slope of $\alpha = 1.67$; the 68% and 90% confidence intervals are equal to [1.49, 1.84] and [1.38, 1.96], respectively (see Table 3). The normalization K is determined by rescaling the model to the actual number of objects in the sample; in the case of the best-fit model, $K = 2.85 \times 10^{-21}$ deg^{-2}. The two dotted lines in Figure 2 represent the $\pm 68\%$ confidence intervals on the slope. A consistent best-fit model is obtained if we consider only the 26 detected sources with a S/N ratio greater than 5 and the corresponding sky coverage ($\alpha = 1.71 \pm 0.26$, $K = 8.28 \times 10^{-22}$ deg^{-2}).

TABLE 3

THE log $(N>S)$–log S FIT PARAMETERS

Fit	α	K (deg^{-2})
−90%	1.38	1.04×10^{-17}
−68%	1.49	4.45×10^{-19}
Best Fit	1.67	2.85×10^{-21}
+68%	1.84	1.52×10^{-23}
+90%	1.96	4.76×10^{-25}

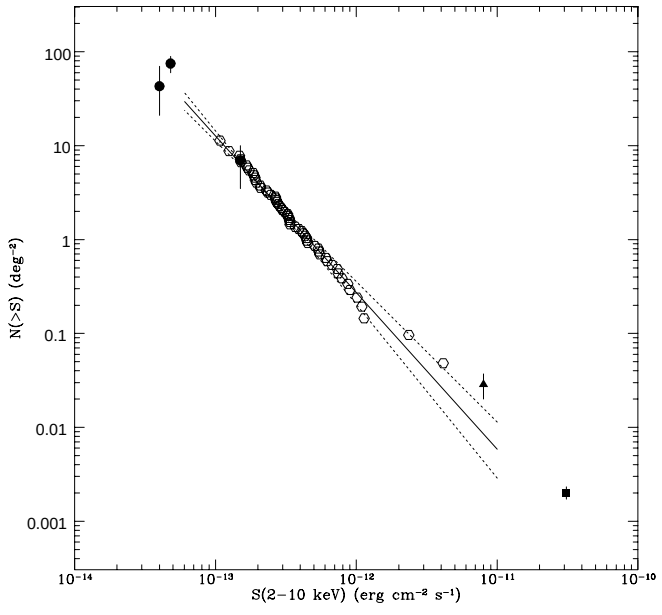

FIG. 2.—Nonparametric (*open circles*) representation of the number-flux relationship obtained with the selected sample. The parametric representation (*solid line*) is well described by a power-law model, $N(>S) = K \times S^{-\alpha}$, with best-fit value for the slope of $\alpha = 1.67 \pm 0.18$ and $K = 2.85 \times 10^{-21}$ deg^{-2}. The dotted lines represent the $\pm 68\%$ confidence intervals on the slope. The filled square represents the extragalactic surface density in the Piccinotti et al. (1982) sample, corrected for the 20% excess of sources due to local superclusters (as estimated by Comastri et al. 1995). The filled triangle represents the results obtained by Kondo (1991) using *Ginga* data. The filled dots are preliminary results of an ongoing *ASCA* survey program conducted on a more limited sky area (Inoue et al. 1996; Georgantopoulos et al. 1997).

The filled square at $\sim 3 \times 10^{-11}$ ergs cm^{-2} s^{-1} represents the surface density of the extragalactic population in the Piccinotti et al. (1982) sample, corrected for the 20% excess of sources due to local superclusters (as estimated by Comastri et al. 1995).

The filled triangle at $\sim 8 \times 10^{-12}$ ergs cm^{-2} s^{-1} represents the surface density of X-ray sources, as determined by Kondo et al. (1991) using a small sample of 11 sources extracted from the *Ginga* high Galactic latitude survey.

Finally, the surface densities represented by the filled dots at $\sim 2 \times 10^{-13}$ ergs cm^{-2} s^{-1} and $\sim 4 \times 10^{-14}$ ergs cm^{-2} s^{-1} are preliminary results from an ongoing *ASCA* survey program conducted on a more limited area of sky (as reported in Inoue et al. 1996), while the filled dot at $\sim 5 \times 10^{-14}$ ergs cm^{-2} s^{-1} is a recent result obtained by Georgantopoulus et al. (1997) using three deep *ASCA*/GIS observations.

Consistent results (at a flux limit of $\sim 6 \times 10^{-14}$ ergs cm^{-2} s^{-1}) are obtained using data from the *BeppoSAX* deep surveys (P. Giommi 1997, private communication).

Figure 2 shows that we have extended the description of the (2–10 keV) number-flux relationship by a factor ~ 450 with respect to the Piccinotti et al. (1982) determination, with a sample of similar size.

We can now evaluate directly from the source counts the contribution of the resolved sources to the 2–10 keV CXB. This contribution is the ratio of the background surface brightness to the emissivity of the objects under study, which is obtained via integration of the observed log $N(>S)$–log S relation.

In the 2–10 keV energy range, the spectrum of the CXB can be described by a power-law representation with an energy spectral index of 0.4 and a normalization of 8 keV cm^{-2} s^{-1} sr^{-1} keV^{-1} (see the review of Hasinger 1996), implying a background surface brightness of ~ 32.87 keV cm^{-2} s^{-1} sr^{-1}.

The emissivity of the resolved objects, $I_{\rm obj}$, is given by

$$I_{\rm obj} = \int_{S_{\rm min}}^{\infty} S \times N(S) dS \ ,$$

where S is the source flux, $N(S)dS$ is the differential representation of the number-flux relationship, and $S_{\rm min}$ is the limiting flux considered.

Using the log $N(>S)$–log S best-fit model (and the $\pm 68\%$ confidence interval) and $S_{\rm min} = 6.3 \times 10^{-14}$ ergs cm^{-2} s^{-1}

(the flux limit of the survey), we obtain $I_{obj} = 8.8^{+0.6}_{-0.2}$ keV cm^{-2} s^{-1} sr^{-1}, which represents about 27% of the 2–10 keV CXB.

We note that our determination of the total intensity produced by the detected sources is *independent* of the intensity of the CXB, and therefore I_{obj} is not affected by the possible uncertainties that could affect estimates of the CXB.

The log $N(>S)$–log S best-fit model implies saturation of the 2–10 keV CXB at a flux of $\sim 8.7 \times 10^{-15}$ ergs cm^{-2} s^{-1}. Therefore, deeper X-ray surveys in this energy range (e.g., the *BeppoSAX*, *Jet-X*, and *XMM* deep surveys) should find a flattening of the number-flux relationship in the range $\sim 8.7 \times 10^{-15}$–$\sim 6.3 \times 10^{-14}$ ergs cm^{-2} s^{-1}, i.e., within a factor of ~ 10 from the present flux limit.

4. DISCUSSION AND CONCLUSION

It is clear that a decisive and final understanding of the real nature of the hard X-ray sources in this sample must await their spectroscopic identification.

In the meantime, we can infer useful information about their nature by comparing the measured 2–10 keV log $N(>S)$–log S with that extrapolated from the soft energy band and with predictions obtained from population synthesis models.

In Figure 3, we display the log $N(>S)$–log S obtained in this work along with 1) the soft (0.5–2.0 keV) log $N(>S)$–log S (Hasinger et al. 1993) extrapolated to the 2–10 keV energy band, assuming a power-law spectral model with energy indices of 1, 0.7, 0.4, and 0.2 (*dotted lines*), and 2) the prediction of the Comastri et al. (1995) model, which is based on the unification scheme of AGNs (*solid line*).

We will discuss these comparisons and their implications in turn.

The first comparison clearly shows a well-known problem (see, e.g., Warwick & Stewart 1989): if we estimate the hard X-ray log $N(>S)$–log S by extrapolating the soft X-ray log $N(>S)$–log S using the mean spectral properties of the sources, as determined in the soft (0.5–2.0 keV) energy band ($\alpha \sim 0.7$–1.2; see, e.g., Almaini et al. 1996), we fail to reproduce it. In particular, at a flux on the order of 10^{-13} ergs cm^{-2} s^{-1}, we predict a surface density that is at least a factor of ~ 2 less than the observed one.

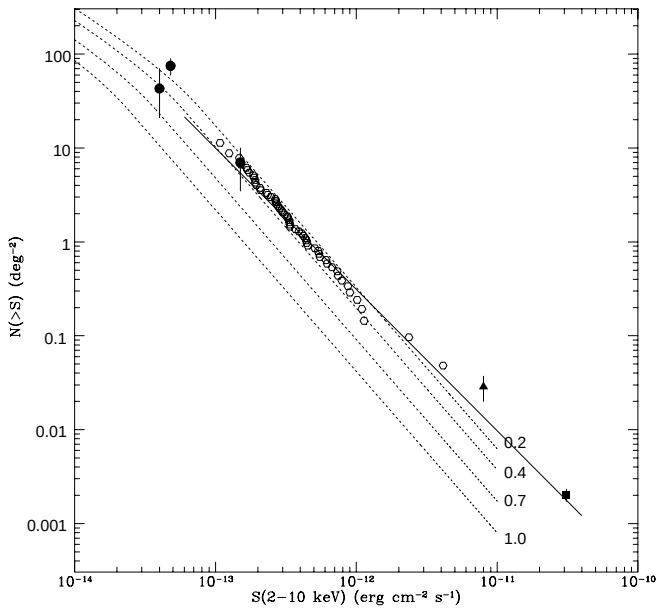

FIG. 3.—Comparison of the derived log $N(>S)$–log S (*open circles*) with the soft (0.5–2.0 keV) log $N(>S)$–log S (Hasinger et al. 1993) extrapolated in the 2–10 keV energy band, assuming a power-law spectral model with energy indices of 1, 0.7, 0.4, and 0.2 (*dotted lines*). The solid line represents the prediction of the Comastri et al. (1995) model.

If the same sources are responsible for both the soft and hard X-ray log $N(>S)$–log S, their average spectral energy index should be on the order of 0.3.

Since at fluxes brighter than $\sim 10^{-13}$ ergs cm^{-2} s^{-1} the principal contribution to the source counts in the soft energy band is from broad-line AGNs (Seyfert 1 and QSOs), we should see a drastic change in their mean spectral properties going from the soft to the hard energy band. This hypothesis seems to be contradicted by the observations (see, e.g., Comastri et al. 1992; Wlliams et al. 1992; Matsuoka & Cappi 1996; Cappi et al. 1997).

An alternative hypothesis is that in the hard energy band we are selecting a population of sources that is actually undersampled in the soft X-ray surveys (e.g., the heavily absorbed AGNs in the Madau, Ghisellini, & Fabian 1994 and Comastri et al. 1995 models). In this respect, it is worth noting the discovery (Ohta et al. 1996) of a type 2 QSO at $z = 0.9$ in an *ASCA*/SIS observation of the Lynx field.

The model of Comastri et al. (1995) is based on the X-ray properties of the unification scheme of AGNs; according to this model, a population of absorbed and unabsorbed AGNs, when folded with the cosmological evolution properties determined in the soft X-ray energy band, is capable of reproducing the shape and intensity of the CXB from several keV to ~ 100 keV. As shown in Figure 3, the predicted 2–10 keV log $N(>S)$-log S of Comastri et al. (1995) (*solid line*) in the flux range $\sim 6 \times 10^{-14}$–$\sim 4 \times 10^{-11}$ ergs cm^{-2} s^{-1} is in very good agreement with our determination.

If this model is correct, we can predict that ~ 52 AGNs and ~ 8 clusters of galaxies should be present among the 60 sources of the present sample. The expected composition of the AGN population in this survey as a function of the intrinsic N_H is reported in Table 4. The population of AGN X-ray emitters with intrinsic N_H in the range 10^{23}–10^{24} cm^{-2} is the most interesting finding; according to Comastri et al. (1995), these should produce the largest fraction of the CXB in the 2–100 keV energy range and should be practically invisible in soft X-ray surveys even at the faintest fluxes reachable with current and future X-ray missions.

We are planning to extend the survey by a factor of ~ 2–3 by analyzing all the available and suitable public GIS2 data. In the meantime, we have begun a program to identify the optical counterparts of the X-ray sources. The main

TABLE 4

AGNs PREDICTED BY COMASTRI ET AL. (1995) MODEL

log N_H (cm^{-2})	Predicted AGN
<21	26
21–22	7
22–23	11
23–24	8
24–25	<1

problem with the spectroscopic follow-up is the absolute accuracy of the *ASCA* attitude solution ($\sim 2'$). Fortunately, *ROSAT*/PSPC data are available for most of the selected GIS2 fields, allowing us to greatly reduce the X-ray error circle for many of the X-ray sources associated with unabsorbed AGNs and with clusters of galaxies. A comparison of the *ASCA* and *ROSAT* spectra of the selected sources with that of the CXB is in progress and will be published elsewhere.

We are grateful to A. Comastri, M. Cappi, G. Ghisellini, and A. Wolter for stimulating discussions. We thank the anonymous referee for the careful reading of the manuscript and for useful comments. I. C. acknowledges partial financial support from NASA grant NAG 5-3174. R. D. C. and T. M. acknowledge partial financial support from the Italian Space Agency (ASI).

REFERENCES

Almaini, O., Shanks, T., Boyle, B. J., Griffiths, R. E., Roche, N., Stewart, G. C., & Georgantopoulos, I. 1996, MNRAS, 282, 295
Boyle, B. J., Griffiths, R. E., Shanks, T., Stewart, G. C., & Georgantopoulos, I. 1993, MNRAS, 260, 49
Boyle, B. J., McMahon, R. G., Wilkes, B. J., & Elvis, M. 1995, MNRAS, 272, 462
Boyle, B. J., Shanks, T., Georgantopoulos, I., Stewart, G. C., & Griffiths, R. E. 1994, MNRAS, 271, 639
Branduardi-Raymont, et al. 1994, MNRAS, 270, 947
Butcher, J. A., et al. 1997, MNRAS, in press
Cappi, M., Matsuoka, M., Comastri, A., Brinkmann, W., Elvis, M., Palumbo, G. G. C., & Vignali, C. 1997, ApJ, 478, 492
Comastri, A., Setti, G., Zamorani, G., Elvis, M., Giommi, P., Wilkes, B., & McDowell, J. C. 1992, ApJ, 384, 62
Comastri, A., Setti, G., Zamorani, G., & Hasinger, G. 1995, A&A, 296, 1
Fabian, A. C. 1989, in Proc. 23d ESLAB Symp. Vol. 2, AGN and the X-Ray Background, ed. N. White, J. Hunt, & B. Battrick (Paris: ESA), 1097
Fabian, A. C., & Barcons, X. 1992, ARA&A, 30, 429
Georgantopoulos, I., Stewart, G. C., Blair, A. J., Shanks, T., Griffiths, R. E., Boyle, B. J., Almaini, O., & Roche, N. 1997, MNRAS, in press
Giacconi, R., Gursky, H., Paolini, F., & Rossi, B. 1962, Phys. Rev. Lett., 9, 439
Gioia, I., Maccacaro, T., Schild, R., Wolter, A., Stocke, J. T., Morris, S. L., & Henry, J. P. 1990, ApJS, 72, 567
Griffiths, R. E., & Padovani, P. 1990, ApJ, 360, 483
Griffiths, R. E., Della Ceca, R., Georgantopoulos, I., Boyle, B. J., Stewart, G. C., Shanks, T., & Fruscione, A. 1996, MNRAS, 281, 71
Griffiths, R. E., Georgantopoulos, I., Boyle, B. J., Stewart, G. C., Shanks, T., & Della Ceca, R. 1995, MNRAS, 275, 77
Gruber, D. E. 1992, in X-Ray Background, ed. X. Barcons & A. C. Fabian (Cambridge: Cambridge Univ. Press), 44
Hasinger, G. 1996, MPE Rep., 263, 291
Hasinger, G., Burg, R., Giacconi, R., Hartner, G., Schmidt, M., Trumper, J., & Zamorani, G. 1993, A&A, 275, 1
Ikebe, Y., Ishisaki, Y., Kubo, H., Idesawa, E., Takahashi, T., Makishima, K., & The GIS Team. 1995, in *ASCA* News 3 (Greenbelt: Goddard Space Flight Center), 13
Inoue, H., Kii, T., Ogasaka, Y., Takahashi, T., & Ueda, Y. 1996, MPE Rep., 263, 323
Jones, L. R., et al. 1997, MNRAS, in press
Kondo, H. 1991, Ph.D. thesis, Univ. Tokyo
Kubo, H., Ikebe, Y., Makishima, K., & The GIS Team. 1994, in *ASCA* News 2 (Greenbelt: Goddard Space Flight Center), 14
Maccacaro, T., et al. 1994, Astrophys. Lett. Commun., 29, 267
Madau, P., Ghisellini, G., & Fabian, A. C. 1994, MNRAS, 270, L17
Marshall, F., et al. 1980, ApJ, 235, 4
Mather, J. C., et al. 1994, ApJ, 420, 439
Matsuoka, M., & Cappi, M. 1996, Mem. Soc. Astron. Italiana, 67, 493
Ohta, K., Yamada, T., Nakanishi, K., Ogasaka, Y., Kii, T., & Hayashida, K. 1996, ApJ, 458, L57
Piccinotti, G., et al. 1982, ApJ, 253, 485
Primini, F. A., Murray, S. S., Huchra, J., Schild, R., & Burg, R. 1991, ApJ, 374, 440
Rosati, P., Della Ceca, R., Burg, R., Norman, C., & Giacconi, R. 1995, ApJ, 445, L11
Setti, G., & Comastri, A. 1996, in IAU Symp. 168, Examining the Big Bang and Diffuse Background Radiations, ed. M. Kafatos & Y. Kondo (Dordrecht: Kluwer), 263
Setti, G., & Woltjer, L. 1989, A&A, 224, L21
Serlemitsos, P. J., et al. 1995, PASJ, 47, 105
Shanks, T., Georgantopoulos, I., Stewart, G. C., Pounds, K. A., Boyle, B. J., & Griffiths, R. E. 1991, Nature, 353, 315
Stocke, J. T., et al. 1991, ApJS, 76, 813
Tanaka, Y., Inoue, H., & Holt, S. S. 1994, PASJ, 46, L37
Vikhlinin, A., Forman, W., Jones, C., & Murray, S. 1995, ApJ, 451, 553
Warwick, R., & Stewart, G. 1989, in Proc. 23d ESLAB Symp. Vol. 2, AGN and the X-Ray Background, ed. N. White, J. Hunt, & B. Battrick (Paris: ESA), 727
Williams, O. R., et al. 1992, ApJ, 389, 157
Zdziarski, A. A., Zycki, P. T., Svensson, R., & Boldt, E. 1993, ApJ, 405, 125